Real-time chromatin dynamics at the single gene level

during transcription activation

Thomas Germier[1, $], Silvia Kocanova[1, $], Nike Walther[2], Aurélien Bancaud[3], Haitham Ahmed Shaban[1], Hafida Sellou[1], Antonio Zaccaria Politi[2], Jan Ellenberg[2], Franck Gallardo[1, 4,5] and Kerstin Bystricky [1, 4,#]

1 : Laboratoire de Biologie Moléculaire Eucaryote (LBME); Centre de Biologie Intégrative (CBI); Université de Toulouse; CNRS; UPS; 31062 Toulouse, France
2: European Molecular Biology Laboratory (EMBL); Heidelberg, Germany
3: Laboratoire de Automatismes et Architecture des Systèmes(LAAS); CNRS; UPS; 31000 Toulouse, France
4: Institut des Technologies Avancées du Vivant (ITAV); Université de Toulouse; CNRS; UPS; INSA; 31000 Toulouse, France
5:NeoVirTech S.A.; 31000 Toulouse, France
$: authors contributed equally
#: corresponding author; bat. IBCG, 118 route de Narbonne, F-31062 Toulouse

Abstract

Genome dynamics relate to regulation of gene expression, the most fundamental process in biology. Yet we still do not know whether the very process of transcription drives spatial organization and chromatin conformation at specific gene loci. To address this issue, we have optimized the ANCHOR/ParB DNA labeling system for real-time imaging and quantitative analysis of the dynamics of a single-copy transgene in human cells. Transcription of the transgene under the control of the endogenous Cyclin D1 promoter was induced by addition of 17β-estradiol. Motion of the ANCHOR3-tagged DNA locus was recorded in the same cell prior to and during appearance of nascent mRNA visualized using the MS2 system. We found that transcription initiation resulted in rapid confinement of the mRNA-producing gene. The confinement was maintained even upon inhibition of pol2 elongation. It did not occur when recruitment of pol2 or transcription initiation was blocked by anti-estrogens or Triptolide. These results suggest that preinitiation complex formation and concomitant reorganization of the chromatin domain constrains freedom of movement of an induced gene's promoter within minutes. Confined diffusion

30   reflects assembly of functional protein hubs and DNA processing during the rate-limiting steps of

31   transcription.

32

33   **Introduction**

34   3D organization of the genome contributes significantly to regulation of major nuclear processes.

35   Changes in average position of chromosome loci in a population of cells correlate with local or global

36   changes in DNA metabolism (Therizols et al. 2014; Taddei et al. 2006; Kocanova et al. 2010; Cabal et al.

37   2006; Chambeyron and Bickmore 2004; Osborne et al. 2004; Schuettengruber and Cavalli 2009; Robinett

38   et al. 1996; Chuang et al. 2006a). This is notably the case for gene transcription, where active genes tend

39   to associate with clusters of RNA polymerase II (pol2) (Feuerborn and Cook 2015). By imaging pol2, its

40   cofactors and mRNA these transcription hubs have been shown to be relatively immobile (Kimura et al.

41   2002; Ghamari et al. 2013; Cisse et al. 2013; Darzacq et al. 2007), but the motion of the associated DNA

42   has not been reported. Consequently, neither do we know if the observed reduced protein mobility is an

43   intrinsic property of the transcription machinery or an indirect effect of changes in chromatin

44   conformation, nor what the precise kinetics of this reorganization at short timescales are.

45   Indeed, real time analysis of chromatin at short time scales relevant for the analysis of transcription

46   activation (minutes) has been hampered by methodological limitations. Existing technologies to visualize

47   DNA loci usually rely on highly repetitive sequences, based on insertion of hundreds of repeats of

48   bacterial operator sequences to which fluorescent repressor fusion proteins bind with high affinity

49   (called FROS for fluorescent repressor operator system (Straight et al. 1996)), or using multiplexed short

50   guide RNAs that stably recruit catalytically inactive dCas9-GFP fusion proteins to a large, repetitive

51   genomic region and partially unwind the target DNA sequence (Chen et al. 2013; Ma et al. 2015). These

52   technologies confirmed that transcription impacts nuclear localization of gene domains. However, they

53   do not allow tagging of genes within immediate vicinity of regulatory elements by fear to disturb their

54 very function. Nevertheless, it was shown that, in yeast, the mobility of a gene was increased by

55 permanently recruiting the potent activator VP16 or chromatin remodeling factors (Neumann et al.

56 2012). This effect could stem from constitutive local decondensation of chromatin near the labelled

57 gene. In mouse ES cells, in contrast, it was reported that in the presence of trans-activation by expressing

58 Nanog, overall gene motion was reduced (Ochiai et al. 2015). In both studies gene motion was compared

59 in different cells. To truly assess immediate changes in chromatin motion during transcription activation,

60 DNA dynamics of a single-copy gene has to be analyzed in real-time while simultaneously monitoring

61 steps of mRNA synthesis in the same cell.

62 To achieve this, we developed a novel ANCHOR (ParB/INT) DNA labeling system (ANCHOR3) for use in

63 human cells. Stable insertion of the ANCHOR3 system into cells in which transcription of target genes can

64 be activated under physiological conditions enables fluorescence imaging of a single locus in the same

65 cell over time, without interfering with gene expression.

66 We demonstrate that the optimized ANCHOR3 system in combination with the MS2 system is ideally

67 suited for simultaneous visualization of DNA and mRNA at a single gene level in living human cells at high

68 spatio-temporal resolution. We show that transcription initiation, not elongation, constrains local

69 displacement of the hormone-induced Cyclin D1 gene as an immediate response to the transcription

70 process in human cells.

71

72

73 **Results**

74 To simultaneously visualize DNA and mRNA of a gene, we labeled a Cyclin D1 (CCND1) transgene with a

75 new, improved ANCHOR3 system (see materials and methods). The ANCHOR system was derived from

76 prokaryotic chromosome partitioning components and originally implemented in yeast (Saad et al.

77 2014). Specific association of a few ParB/OR protein dimers to a limited number of parS binding sites

3

78   within the bacterial chromosome's partitioning site initiates formation of a large nucleoprotein complex

79   dependent on non-specific, dynamic ParB/OR binding and ensuing oligomerization (Passot et al. 2012;

80   Graham et al. 2014; Sanchez et al. 2015)**. The ANCHOR system thus relies simply on a short ANCH/INT

81   sequence (<1kb) that can be inserted immediately adjacent, within a few base-pairs, to regulatory

82   elements.

83   The transgene is further composed of the endogenous CCND1 promoter, a CCND1 cDNA cassette

84   including its 3'enhancer region and 24 repeats of the MS2 MCP protein–binding sequence within the

85   CCND1 3'-UTR (Yunger et al. 2010) (Fig. 1a). The construct was inserted into an FRT site within the

86   genome of estrogen receptor *alpha* (ERα)-positive MCF-7 human mammary tumor cells (Fig. 1a). In the

87   engineered, monoclonal cells, called ANCH3-CCND1-MS2, fluorescent OR3-fusion proteins form a single

88   focus at the ANCH3 site of the transgene that can be readily tracked in real time (Fig. 1b; Videos S1, S2).

89   To characterize the binding kinetics of OR3 proteins at and around the ANCH3 site, we used fluorescence

90   recovery after photo-bleaching (FRAP) of OR3-EGFP labeled spots (Fig. 1b). Association and dissociation

91   of OR3-EGFP at the ANCH3-tagged site was in a dynamic steady state with a measured half-life of 57±2s

92   (Fig. 1b). To estimate the copy number of OR3 proteins at an ANCH3 site in steady state, we performed

93   confocal imaging calibrated by fluorescence correlation spectroscopy (FCS), which allowed us to convert

94   pixel fluorescence intensity to protein concentration or number (Fig. S1a-e). The fluorescence intensity

95   of the ANCHOR3 spot increased with OR3-EGFP abundance (Fig. S1f). Under our OR3 expression

96   conditions, we calculated an average of 481 ± 274 fluorescent molecules per site, corresponding to a

97   significant amplification of the nine OR3 dimers bound specifically to the parS sites of the ANCH3

98   sequence (Fig. S1f).

99   The MCP-EGFP signal corresponding to accumulated CCND1 transcripts is detectable near the ANCHOR3-

100   labeled DNA site 45 minutes after 17β-estradiol (E2) addition to G1-synchronized cells grown in steroid-

101   stripped media (Fig. 1c; video S2), consistent with the fact that ERα target gene expression is triggered 10

4

102　　minutes after E2 addition (Hah et al. 2011; Métivier et al. 2003). Thus, the engineered cell line enabled

103　　real-time imaging of a single copy gene during transcription activation by the endogenous ERα, under

104　　physiological conditions.

105　　To directly test whether changes in gene expression impact local chromatin dynamics, we recorded the

106　　motion of the fluorescent ANCHOR3-Santaka-tagged gene in the same cell prior to and 45 min after

107　　adding 100nM E2, while monitoring the appearance of MCP-EGFP-labelled mRNA signals (Fig. 1c). Live

108　　cell tracking revealed that movement of the CCND1 gene is locally constrained upon induction of its

109　　transcription (Fig. 1d, table 1). We quantified the average displacement of the tagged transgene by

110　　plotting the mean square displacement (MSD) to each time interval Δt (see materials and methods).

111　　MSD curves calculated from time-lapse image series acquired with an inter-frame interval of 250 ms for

112　　a total of 50 s are shown in Fig. 2a. We found that MSD plots of E2-activated CCND1 differed significantly

113　　from those of non-activated cells (Fig.2a left panels, Fig. S2, S3). In contrast, E2 had no effect on the

114　　behavior of a non-genic ANCH3-only construct integrated at the same genomic location (Fig. 2a right

115　　panels, Fig. S2, S3), confirming that the measured decline in mobility was due to transcription of the

116　　transgene rather than to unspecific, genome-wide effects of hormone addition. We also examined the

117　　motion of the ANCH3-CCND1-MS2 or ANCH3-only constructs inserted into distinct chromosomes (G7,

118　　A11 and D11 clones; Fig. 2a, Fig. S2). At the single cell level, we recorded large variations in MSD of the

119　　transgene in all clones, but these variations did not correlate with any specific insertion site (Fig. S2).

120　　Intriguingly, motion of the ANCH3-tagged single gene locus followed two distinct regimes with an

121　　increase in the slope of the recorded MSD at time intervals >5 s in these human mammary tumor cells

122　　synchronized in G1 (Fig. 2b left panel, Fig. S2). The average MSD curves over 21 trajectories followed a

123　　non-linear, anomalous diffusive behavior characteristic of objects moving in complex environments such

124　　as the nucleoplasm (Saxton 2009)(Fig. S2). Hence, we analyzed these MSDs on the basis of a generalized

125　　diffusion model obeying a power law $MSD \sim k\tau^{\alpha}$ with k as prefactor, t the time interval, and α the

5

126   anomalous diffusion exponent, a model shown to reflect chromatin motion in several cell types and

127   under various conditions (Manzo and Garcia-Parajo 2015). Applying this model to our data, we

128   demonstrate that at short <5 s time intervals diffusion of the chromatin fiber of a single gene domain is

129   highly anomalous (α <0.4) and subjected to local constraints. At greater time intervals, the slope of the

130   population averaged MSD curve increases (α~1) suggesting that the fiber of the non-transcribed gene

131   locus (ANCH3-CCND1-MS2 or ANCH3 only) is rather mobile, almost freely diffusing. In contrast, the

132   dynamic behavior of the mRNA producing CCND1 loci differs significantly: the MSD slope remains low (α

133   ~0.5) consistent with significant confinement of the actively transcribed locus (Fig. 2b).

134   To fully exploit our ability to track a single gene, we computed an average squared displacement from 2s

135   to 40 s (mean MSD) before and after induction of transcription in the same cell. For both constructs, in

136   the absence of E2, the mean MSD ranged from 0.009 to 0.290 μm^2 (Fig. 2c). This heterogeneity in the

137   amplitude of motion is coherent with variations in the nuclear environment owing to crowding in

138   mammalian nuclei (Hancock 2004; Huet et al. 2014; Ochiai et al. 2015). Independently of the initial

139   mobility, mean MSDs recorded for each cell producing MCP-labeled mRNA were consistently reduced

140   after addition of E2 to ANCH3-CCND1-MS2 cells (Fig.2c left panel; between 0.006 and 0.090μm^2; n=15; p-

141   value=0.006). In contrast, variations in mean MSD of the non-genic ANCH3 locus were not significantly

142   affected by E2 addition (Fig. 2c right panel; n=21; p-value=0.3).

143   To more accurately describe the behavior of the tracked chromatin locus, we determined its area of

144   confinement, track length and speed in addition to time averaged MSDs which suffer from

145   approximating experimental errors (Kepten et al. 2015). We found that spatial confinement of the

146   transcribed locus reflected obstructed diffusion. The nuclear area explored by the tagged locus over a 50

147   s time interval in the absence of hormone was reduced by 33% upon addition of E2, from 0.175 ±0.119

148   μm^2 (n=63, no E2, no detectable MCP labeled mRNA) to 0.117 ±0.006μm^2 (n=34; visible mRNA

149   accumulation at the tagged locus after 45 min E2) (Fig. 2d, table 1). Surprisingly, the mean step size of

6

150   the tracked locus was greater after E2 addition (Fig. 2e) and, as a consequence, the apparent velocity of

151   the transcribed CCND1 locus increased from 0.26 µm/s to 0.29 µm/s (table 1). The ANCH3-only locus did

152   not alter its speed in the presence of E2 (table 1).

153   Confinement of the chromatin fiber could stem from steric hindrance due to protein loading or a change

154   in the physical parameters of the fiber, or both (Banks and Fradin 2005). We first tested whether

155   recruitment of large transcriptional co-factor complexes by hormone-bound ERα to the CCND1 promoter

156   could influence chromatin mobility. Similarly to E2, Tamoxifen (OH-Tam) triggers ERα binding to

157   responsive promoters, which leads to recruitment of numerous proteins and chromatin remodeling

158   complexes; in contrast to E2, OH-Tam-bound ERα attracts transcriptional co-repressors (Shang et al.

159   2000; Liu and Bagchi 2004). However, changes in the recorded amplitude of the MSD calculated from

160   tracking the ANCH3-tagged CCND1 locus after addition of 1µM OH-Tam did not show a distinct trend.

161   Motion was variable and similar to the dynamic behavior of the constructs in the absence of hormone

162   (Fig. S3). We conclude that association of a multitude of transcriptional co-factors recruited by OH-Tam-

163   bound ERα alone, in the absence of transcription, cannot explain local confinement of the chromatin

164   fiber.

165   We next assessed the role of pol2 activity on motion of the tagged CCND1 locus using two distinct pol2

166   inhibitors (Fig. 3). E2-stimulated cells were treated with an elongation-inhibitor, the adenosine analogue

167   5,6-dichloro-1-β-D-ribofuranosylbenzimidazole (DRB). CCND1 mRNA signals disappeared 30 min after

168   addition of 50µM DRB to ANCH3-CCND1-MS2 cells indicating that completion of elongation, i.e.

169   transcription of the 3'UTR including MS2 repeats, was efficiently inhibited (Fig. 3b). The appearance of

170   the MSD plot of the CCND1 locus tracking after DRB addition to cells maintained in E2-containing

171   medium was similar to the one in cells which had not been treated with DRB (Fig. 3b, single cell MSD

172   curves), suggesting that confined motion was sustained despite blocking elongation. Mean MSD values

173   and area of confinement for several cells analyzed 45 min after E2 stimulation and 30 min after adding

7

174   DRB did also not change significantly (Fig. 3c, table 1). When pre-treating cells for 30 min by DRB prior to

175   adding hormone, we again observed a rapid decline in CCND1 motion upon mRNA production in every

176   single cell analyzed (Fig. 3d). It is further known that in DRB-treated cells, transcription initiation by pol2

177   is preserved but elongation aborts rapidly within the first transcribed exon (Gribnau et al. 1998). Our

178   observations let us speculate that initiating but not elongating pol2 confines chromatin dynamics locally.

179   To confirm this hypothesis, we analyzed the tagged gene's motion in cells treated with 500 nM Triptolide

180   (TPL), an inhibitor of TFIIH that blocks pol2 at the promoter after PIC assembly (Vispé et al. 2009; Jonkers

181   et al. 2014) (Fig. 3a). Addition of TPL to E2-stimulated mRNA-producing cells released the constraint as

182   the MCP-GFP signal diffuses away from the ANCH3-tagged transgene (Fig. 3e). Indeed, mean MSD values

183   of the ANCHOR3 spot's track increased after 30 min or 60 min depending on efficiency of TPL for evicting

184   pol2 from the gene body (Fig. 3f, table 1). Addition of E2 to TPL pre-treated cells had no impact on the

185   recorded motion of the transgene (Fig. 3g, table 1). Hence, our data suggest that events linked to PIC

186   initiation induce changes in chromatin mobility, leading to increased local velocity at time scales > 5s

187   within a largely confined area.

188

189   **Discussion**

190   Real-time tracking of a single-copy Cyclin D1 gene in the same cell prior to and during hormone-induced

191   mRNA synthesis revealed that transcription initiation rapidly confines the mRNA-producing gene and

192   alters its diffusive behavior. Confinement was maintained even upon inhibition of pol2 elongation, but

193   did not occur when recruitment of pol2 or transcription initiation was blocked by anti-estrogens or

194   Triptolide. Our results suggest that PIC formation and concomitant reorganization of the chromatin

195   domain constrain freedom of movement of an induced gene's promoter within minutes, compatible with

196   the establishment of a transcriptional hub. Indeed, pol2 aggregates in numerous rather immobile foci

197   (Cisse et al. 2013; Darzacq et al. 2009). Several models concur in saying that a small fraction of active

8

198   pol2 forms clusters with reduced mobility as transcription initiates (Stasevich et al. 2014; Kimura et al.

199   2002; Cisse et al. 2013). This clustering is dependent on the presence of initiating pol2 complexes

200   (Mitchell and Fraser 2008). But what causes pol2 to stop moving? In principle, our observation that

201   transcription initiation locally confines chromatin dynamics within minutes is compatible with the idea

202   that pol2 foci assemble at active genes, and that, as the transcription initiation bubble forms, a decline in

203   DNA freedom of movement leads to reduced pol2 mobility.

204   Regulation of the CCND1 locus has been shown to involve intragenic looping (Dalvai et al. 2013). Such

205   conformational changes in gene domain organization, similar to those observed during glucocorticoid

206   stimulated transcription of MMTV tandem array gene loci in mouse adenocarcinoma cells (Stavreva et al.

207   2015), are likely to have direct consequences for chromatin dynamics. For instance, the anchoring of

208   several chromosome fibers within pol2 foci may increase the drag coefficient and hence reduce

209   chromatin displacements. The changes in local dynamics we describe are thus compatible with

210   reorganization of pre-existing chromatin folding within the gene domain at the 100 kb range via long-

211   range looping (Mourad et al. 2014; Chuang et al. 2006b; Therizols et al. 2014). Greater local velocity of

212   the transcribed locus might increase the frequency of interaction with transcriptional cofactors and

213   polymerases of the gene within its regulatory compartment similar to what was recently modelled as a

214   'nanoreactor'(Haddad et al. 2017). Increased collisions are compatible with the formation of gene

215   domain specific chromatin clustering (also called 'topologically associated domains' or TADs) readily

216   detected by crosslinking methods in mammary tumor cells (unpublished;(Le Dily et al. 2014; Giorgetti et

217   al. 2014). In turn, confined dynamics may prevent formation of unwanted long range contacts as

218   transcription proceeds.

219

220   At the sub-megabase level, TADs comprise one or a few open reading frames and their regulatory

221   elements (gene domains) (Ulianov et al. 2016), particularly in human mammary tumor cells (Barutcu et

222   al. 2016; Mourad et al. 2014; Le Dily et al. 2014; Fullwood et al. 2009)(Kocanova et al. in preparation). If

223   the existence of TADs is elusive in yeast, increased ligation frequencies also occur around gene bodies at

224   the 2 kb range (Hsieh et al. 2015). Most of our knowledge of chromatin dynamics stems from work in

225   budding yeast (Bystricky 2015; Botstein and Fink 2011; Wang et al. 2015; Taddei and Gasser 2012). In

226   particular, live cell chromatin motion of a series of tagged genomic yeast loci fits a Rouse model of

227   polymer dynamics, in which the MSD increases with time with a power-law scaling and an anomaly

228   exponent $\alpha \sim 0.5$ (Hajjoul et al. 2013). Assuming that within a ~100 kb chromatin domain around any of

229   the tagged sites, at least one gene is actively transcribed in a population of yeast nuclei, the reported

230   dynamic behavior characterizes active chromatin. In agreement, obstructed diffusion characterizes the

231   active CyclinD1 transgene locus in human cells here. In the absence of transcription the tagged single

232   human transgene domain was highly dynamic, nearly freely diffusing. Similarly, our unpublished

233   observations in yeast evidence increased motion when mutating RNA pol 2 (Mathon, Wang et al. in

234   preparation). Transcription-induced, pol2 dependent, intra-domain contacts therefore likely result from

235   the apparent highly diffusive behavior of chromatin in living cells. Anomalous diffusion was also reported

236   for telomeres (Bronshtein et al. 2015) and for gene arrays (Annibale and Gratton 2015) but changes were

237   derived from comparing motion in cells monitored under different conditions. The computed MSD

238   curves of these loci characterized by specific structures differ from the ones we compute for a single

239   gene locus which emphasizes the need for future modeling to better define physical parameters of the

240   chromatin fiber in human cells.

241   Because dynamic properties of chromatin have been implicated in all fundamental cellular processes we

242   propose that decrease in chromatin motion as a consequence of transcription initiation confers essential

243   functions to chromatin dynamics. The powerful real-time imaging approach of a single DNA locus

244   undergoing functional changes presented here using the ANCHOR system is widely applicable to other

245   loci and genomes for studying rapid biological processes with single cell resolution, and completing the

246   picture emerging from imaging RNA pol2 and mRNA, but also from chromosome conformation capture

247   data.

248

249   **Materials and Methods**

250   **Cell line**

251   The human breast cancer cell line MCF-7 (purchased from ATCC) was used to generate stable FRT/LacZeo

252   clones. Cells were grown in Dulbecco's modified Eagle medium F-12 (red DMEM/F12) completed with

253   10% FBS (Gibco), 1% Sodium Pyruvate (Gibco) and 0.5% Gentamycine (Gibco) or in phenol red free

254   DMEM/F12 completed with 10% charcoal stripped serum, 1% Sodium Pyruvate (Gibco) and 0.5%

255   Gentamycine (Gibco), in a water-saturated atmosphere containing 5% CO_2 at 37°C. Transfections were

256   carried out using FuGENE HD Transfection Reagent (Promega), according to the supplier's

257   recommendation.

258   **ANCHOR3 labeling system**

259   ANCH3 corresponds to a specific chromosome partition sequence and was amplified directly by PCR

260   from the genome of an undisclosed exotic bacteria *(upon acceptance, name will be disclosed and vectors*

261   *made available for purchase from Addgene)*. The PCR product was then cloned using BamH1/HindIII into

262   pCDNA FRT vector digested by BglII/HindIII (Invitrogen). Insertion was verified by ApaI digestion and

263   sequencing. OR3 corresponding to the cognate ParB protein was amplified by PCR and cloned via

264   BglII/KpnI directly into pGFP-c1 digested by the same enzyme. Insertion was verified by digestion and

265   sequencing. Functionality of the construct was verified by co-transfection of both vectors in Hela cells,

11

266   and produced clearly identifiable fluorescent spots. To construct the ANCH3-CCND1-MS2 transgene (Fig.

267   1a) the ANCH3 sequence was amplified by PCR with primers containing EcoRV restriction sites and

268   ligated into the EcoRV digested pCDNA5-FRT/CCND1pr-HA-CCND1/24MS2/3'UTR plasmid (kindly

269   provided by YaronShav-Tal (Yunger et al. 2010)).

Engineering of stable FRT/LacZeo clones expressing the CCND1 transgene

271   MCF-7 cells were transfected using pFRT//lacZeo kit from Invitrogen according to the supplier's protocol.

272   Selection of FRT clones was performed using 75µg/ml Zeocin (InvivoGen) in red DMEM/F12 medium.

273   Selection medium was renewed every 3 days. Three clones, showing the same growing behavior and

274   ERα-target gene expression profiles as MCF-7 cells were kept for use: G7, A11 and D11. Clones G7, A11,

275   D11 were transfected with 1µg of ANCH3-CCND1-MS2 or ANCH3 plasmids and 6µg of plasmid pOG44

276   encoding Flipase (Invitrogen). Selection of positive clones was performed with 75µg/ml Hygromycin

277   (Invitrogen) and presence of a single fluorescent focus was verified by fluorescence microscopy 24h after

278   cell transfection with 500ng OR3-Santaka. ANCH3-CCND1-MS2 cells as well as control cells with only an

279   ANCH3 insertion were maintained in red DMEM/F12 completed with 75µg/ml Hygromycin.

Fluorescence correlation spectroscopy (FCS) and fluorescence recovery after photobleaching (FRAP)

experiments

282   For FCS and FRAP experiments, 2 x 10^4cells were seeded on 8well Lab-TekI chambered cover glass

283   (Nunc). To visualize spots, cells were transfected 1h after cell seeding with a plasmid encoding OR3-EGFP

284   using FuGENE HD transfection reagent (Promega) according to the manufacturer's instructions for a 3:1

285   transfection reagent:DNA ratio. To express free mEGFP as a control for FCS, cells were transfected 1h

286   after cell seeding with a plasmid encoding mEGFP (kindly provided by J. Lippincott-Schwartz) using

287   FuGene6 transfection reagent (Promega) according to the manufacturer's instructions for a 3:1

288   transfection reagent:DNA ratio. FCS and FRAP experiments were performed 24 to 48h after cell

289   seeding/transfection in CO_2-independent imaging medium (Gibco, custom-made) supplemented with

290   20% (v/v) FBS, 1% (v/v) sodium pyruvate and 1% (v/v) L-glutamine.

291   **Fluorescence recovery after photobleaching (FRAP)**

292   Imaging was performed on a Zeiss LSM780 ConfoCor3 confocal microscope using a 40x, 1.2 NA, water

293   Korr FCS objective. Prior to each FRAP time-lapse, an overview image of the measured interphase cell

294   with a nuclear spot was taken. GFP was excited with a 488 nm laser (Ar, 25 mW, 0.4% AOTF transmission,

295   2.3 µW at probe) and detected with a GaAsP detector using a 492-552 nm detection window (Δx, Δy = 83

296   nm, Δz = 0.4, 60x60 pixels, 9 z-slices). 40 images were acquired at a 5 s time interval. After three pre-

297   bleach images a circular ROI (12 pixels wide) containing the ANCHOR spot was bleached with five

298   iterations and maximal laser power. For bleaching controls, cells with spots were acquired with the same

299   conditions as in the FRAP experiments but without bleaching the fluorescent spot. The z-position was

300   stabilized using Zeiss Definite Focus. Due to hardware limitations the first four images have a time

301   interval between 3.4 s and 6.6 s. These reproducible differences were taken into account in the analysis.

302   The image analysis was performed using FiJi (http://fiji.sc/Fiji). For each FRAP time-course the position of

303   the OR3-EGFP ANCHOR spot was tracked in 3D using the FiJi MOSAIC plugin for 3D single-particle

304   tracking (http://mosaic.mpi-cbg.de/?q=downloads/imageJ,(Sbalzarini and Koumoutsakos 2005)). If a spot

305   was not detectable after photobleaching, its position was interpolated. The mean fluorescence intensity

306   F_s was measured in a 5x5 rectangular region around the tracked spot. The background fluorescence

307   intensity $F_{bg}$was measured from a ROI in the unbleached part of the nucleus. Relative fluorescence

308   intensity RI at time point t_i (Fig. S1d) is given by

$$RI(t_i) = \frac{\left(F_s(t_i) - F_{bg}(t_i)\right)}{\sum_{j=1}^{3}[F_s(t_j) - F_{bg}(t_j)]/3} e^{-k_{bl}t_i}.$$

(Eq. S1)

309   whereby the data was normalized to the average of the first three pre-bleach images and bleach

310   corrected using an exponential factor. The bleaching rate k_{bl} was estimated from the FRAP time-courses

311   without bleaching the ANCHOR3 spots. Overall bleaching was below 10% within the acquired 40 frames.

312   The post-bleach kinetics were fitted to a single exponential function as described in the legend to Fig.

313   S1d.

314   **Fluorescence correlation spectroscopy (FCS) and protein number estimation**

315   Imaging and photon counts were acquired on a Zeiss LSM780 ConfoCor3 confocal microscope using a

316   40x, 1.2 NA, water Korr FCS objective. Cells were imaged (Δx, Δy = 83 nm, Δz = 0.4, 164x164 pixels, 9 z-

317   slices) and subsequently two positions in the nucleus outside of ANCHOR3 spots were selected for FCS at

318   the z-position of the central slice. For imaging, GFP was excited with a 488 nm laser (Ar, 25 mW, 0.4%

319   AOTF transmission, 2.3 µW at probe) and detected with a GaAsP detector using a 492-552 nm detection

320   window. For pre-FCS imaging the same detector settings, pixel size, pixel dwell time, and laser settings

321   were used as for FRAP, allowing the conversion of fluorescence intensities in the first pre-bleach FRAP

322   images to concentrations and protein numbers based on an FCS calibration (Eq. S3). For FCS, GFP was

323   excited with a 488 nm laser (Ar, 25 mW, 0.05% AOTF transmission, 0.28µW at probe) and the photon

324   counts were recorded for 30 s using an avalanche photodiode detector (APD; 505-590 nm detection). To

325   estimate the effective volume, a water solution of Alexa488 (Lifetech) with a known diffusion coefficient

326   (D_{alexa} = 441 µm^{2}sec^{-1}, M. Wachsmuth, EMBL, personal communication) was measured before each

327   experiment.

328   The   raw   photon   counts   were   processed   using   FluctuationAnalyzer   4G

329   (http://www.embl.de/~wachsmut/downloads.html).   This   program   computes   the   autocorrelation

330   function (ACF), correction factors, e.g. due to background, and fits the ACF to physical models of

331   diffusion (see Wachsmuth et al., 2015, for further details). The ACF $G(\tau)$ was fit to

$$G(\tau) = \frac{1}{N}\left[1 - \theta + \theta e^{-\tau/\tau_{trip}}\right]\left[\left(1 + \left(\frac{\tau}{\tau_D}\right)^\alpha\right)^{-1}\left(1 + \frac{1}{\kappa^2}\left(\frac{\tau}{\tau_D}\right)^\alpha\right)^{-\frac{1}{2}}\right].$$

(Eq. S2)

332   Equation S2 describes anomalous diffusion: N denotes the number of particles in the effective volume,

333    $\kappa = 5.5$ the structure factor, i.e. the ratio of axial to lateral radius of the effective volume, τ_D the

334   characteristic diffusion correlation time, α the anomaly parameter. The parameter θ is the fraction of

335   molecules in a non-fluorescent state and τ_{trip} the apparent life-time in this state. The value of τ_{trip} was

336   set to 100 µs and the other parameters were fit to the data.

337   The concentration of molecules in the effective focal volume V_{eff} is given by $C = N/V_{eff}N_A$, where

338    $V_{eff} = \pi^{3/2}\kappa w_0^3$ and N_A is the Avogadro's constant. The lateral focus radius w_0 is given by

339    $w_0 = 2\sqrt{\tau_{alexa}D_{alexa}}$ where τ_{alexa} is the characteristic diffusion correlation time measured for Alexa488.

340   The counts per molecule are given by $CPM = N/\langle I\rangle$, where $\langle I\rangle$ is the average photon counts.

341   For each experiment, a calibration curve (Fig. S1c) was calculated from the mean fluorescence intensity

342   (FI) and the concentration obtained from FCS. The mean FI was measured in a 5x5 px large square at the

343   location of the FCS measurement. The data points were fit to a line that describes the relationship

344   between fluorescence intensity *FI* and concentration *C*:

$$C = a + b\,FI.$$

(Eq. S3)

345   Based on Eq. S3, each pixel of images acquired with the same settings as the pre-FCS images can be

346   converted to a concentration. The protein number in each voxel was obtained by multiplying the

347   concentration *C* with the voxel volume V_{vox} and N_A (see Fig. S1e).

15

348   To estimate the protein number at the ANCHOR site, the first pre-bleach image of the FRAP time-course

349   was used. The FI was converted to protein number per pixel using the calibration curve in Eq. S3 and V_{vox}.

$$N(x,y) = \frac{A}{2\pi\sigma^2}\exp\left(-\frac{(x-x_s)^2}{2\sigma^2} - \frac{(y-y_s)^2}{2\sigma^2}\right) + bg \qquad \text{(Eq. S4)}$$

350   In a 14x14 rectangular region at the location of the ANCHOR3 site a 2D Gaussian was fit (Eq. S4), where x_s

351   and y_s are the coordinates of the spot, bg the background nuclear signal and A the total protein number

352   at the Anchor site. For the fit the Gauss Fit on Spot ImageJ plugin (http://imagej.nih.gov/ij/plugins/gauss-

353   fit-spot/index.html) was used.

354   **Fluorescence live cell imaging under stimulation**

355   For live cell tracking during transcription activation, 80 000 cells were plated in 35mm glass bottom

356   culture plates (Ibidi, Biovalley) in red DMEM/F12 medium and allowed to attach for 24h. Red DMEM/F12

357   medium was changed for phenol red free DMEM/F12 medium supplemented with 10% charcoal stripped

358   serum and cells were kept in the latter medium for 72h. Cells were co-transfected with 500ng

359   OR3-Santaka and 1µg MCP-GFP DNA vectors 24h before observation.

360   To activate transcription of the ANCH3-CCND1-MS2 transgene, cells were maintained in L-15 medium

361   (Liebovitz's, Gibco) supplemented with 10% charcoal stripped serum, a buffer appropriate for live cell

362   imaging.

363   Observations were made using a Nipkow disk confocal system (Revolution; Andor) installed on a

364   microscope (IX-81), featuring a confocal spinning disk unit (CSU22;Yokogawa) and a cooled electron

365   multiplying chargecoupled device camera (DU 888; Andor). The system was controlled using the

366   Revolution IQ software (Andor). Images were acquired using a 60× Plan Apo 1.42 oil immersion objective

367   and a two-fold lens in the optical path. Single laser lines used for excitation were provided diode

368   solid-state lasers exciting GFP fluorescence at 488 nm (50 mW; Coherent) and Santaka fluorescence at

369   561 nm, and a Quad band pass emission filter (Di01-405/488/568/647-13x15x0,5; Semrock) allowed

16

370   collection of the green and redfluorescence. Pixel size was 110 nm. Movies containing 200 image frames

371   acquired with an exposure time of 250ms were recorded. Images were processed using ICY and FIJI

372   software.

373   After imaging of the cells without transcription stimulation, 100nM 17β-estradiol (E2; Sigma) was added

374   directly under the microscope and dynamics of the OR3-Santaka spot in the same cells were recorded

375   45min later. Before acquisition under E2 stimulation, presence of the MCP-GFP foci, indicating active

376   transcription elongation, was verified in each analyzed cell (Fig. 1c). To block transcription elongation, we

377   added fresh L-15 medium containing 50μM DRB (5,6-dichloro-1-β-D-ribofuranosylbenzimidazole; Sigma).

378   The cells were imaged 30min after DRB addition and disappearance of the MCP-GFP foci was verified

379   (Fig. 3b). To examine the impact of transcription initiation on chromatin motion in living cells, we added

380   fresh L-15 medium containing 500nM Triptolide (TPL, Sigma) before or after stimulation by E2. The cells

381   were imaged under the same conditions as for DRB treatment. To study the effect of OH-Tamoxifen (OH-

382   Tam; Sigma), cells were maintained in L-15 medium and imaged before and 45min after 1μM OH-Tam

383   treatment.

384   **Lateral drift test**

385   Lateral drift was analyzed by cross correlation. Cross correlation assumes that shape of the structures

386   imaged in the sample is not expected to change significantly during the acquisition; the structure itself

387   can be used to determine whether spatial shift between subsequent images exists. For single cell

388   analysis, movies were cropped and registered by the ImageJ plug-in StackReg using translation and rigid

389   body functions for drift correction, before tracking of the DNA locus using ICY tracker (*2*). The translation

390   function calculates the amount of translation (Δ**r**) by a vectoring analysis from **x** = **r** + Δ**r**. Where, **x** and **r**

391   are the output and input coordinates. Rigid body transformation is appropriate because coordinates

392   are **x** = {{cos ϑ, −sin ϑ}, {sin ϑ, cos ϑ}} · **r** + Δ**r**, considering both the amount of translation (Δ**r**) and the

393   rotation by an angle ϑ(*2*).

394 **Mean square displacement**

395 Particle tracking experiments and MSD calculations were carried out using ICY and MatLab software.

396 Tracks of 200 frames were scored. OR3-Santaka spots were detected and tracked using the Spot detector

397 and spot tracking plugin from ICY in single cells. Mean square displacements (MSD) were calculated in

398 Matlab using the following equation:

399 $$dl2(j,i)=(x(j+i)-x(i))^2+(y(j+i)-y(i))^2 \qquad \text{(Eq. S5)}$$

400 Averaged MSD resulted from averaging the MSD at each time interval (Fig. 2b, n=14). Mean MSD were

401 extracted from the average squared displacement from 2s to 40 s of the ANCH3 locus during the time of

402 acquisition in one cell (Fig. 2c, 3c, 3d, 3f and 3g, n=15,n=21, n=9, n=7, n=3 and n=10 respectively). Areas

403 of confinement were obtained using the raw trajectories over 50sec and fitted based on an ellipse.

404 **Statistics**

405 Results were analyzed using two different tests. A Student's t-test with a confidence interval of 95% was

406 used for data presented in Fig. 2c, 2d and 2e. A Wilcoxon signed-rank test was used for data presented in

407 Fig. 3c, 3d, 3f and 3g

408

409 **Disclosure**

410 The authors declare no conflict of interest.

411

412

413 **Acknowledgements**

18

418   SystemsMicroscopy NoE (258068) and the 4DN NIH Common Fund (U01 EB021223), NW by the EMBL

419   International PhD Programme (EIPP).

420

421   **Author contributions**

422
423   Performed experiments: TG, SK, FM
424   Analysed data: TG, SK, AB, HSh, KB
425   NW performed and analysed, AZP analysed and JE supervised the FRAP and FCS analysis.
426   Generated material: TG (cell lines), HSe (cell lines, constructs), FG (ANCHOR3 system)
427   Wrote paper: KB, TG, SK;

428

429

430   **References**

431

432   Annibale P, Gratton E. 2015. Single cell visualization of transcription kinetics variance of highly mobile

433   identical   genes   using   3D   nanoimaging.   *Sci   Rep*   **5**:   9258.

434   http://www.nature.com/doifinder/10.1038/srep09258.

435   Banks DS, Fradin C. 2005. Anomalous Diffusion of Proteins Due to Molecular Crowding. *Biophys J* **89**:

436   2960–2971.

437   Barutcu AR, Lajoie BR, Fritz AJ, McCord RP, Nickerson JA, van Wijnen AJ, Lian JB, Stein JL, Dekker J, Stein

438   GS, et al. 2016. SMARCA4 regulates gene expression and higher-order chromatin structure in

439   proliferating   mammary   epithelial   cells.   *Genome   Res*   gr.201624.115.

440   http://genome.cshlp.org/lookup/doi/10.1101/gr.201624.115.

441   Botstein D, Fink GR. 2011. Yeast: An experimental organism for 21st century biology. *Genetics* **189**: 695–

442   704.

443   Bronshtein I, Kepten E, Kanter I, Berezin S, Lindner M, Redwood AB, Mai S, Gonzalo S, Foisner R, Shav-Tal

444   Y, et al. 2015. Loss of lamin A function increases chromatin dynamics in the nuclear interior. *Nat*

19

445   *Commun* **6**: 8044. http://www.nature.com/doifinder/10.1038/ncomms9044.

446   Bystricky K. 2015. Chromosome dynamics and folding in eukaryotes: insights from live cell microscopy.

447   *FEBS Lett*. http://linkinghub.elsevier.com/retrieve/pii/S0014579315006110.

448   Cabal GG, Genovesio A, Rodriguez-Navarro S, Zimmer C, Gadal O, Lesne A, Buc H, Feuerbach-Fournier F,

449   Olivo-Marin J-C, Hurt EC, et al. 2006. SAGA interacting factors confine sub-diffusion of transcribed

450   genes to the nuclear envelope. *Nature* **441**: 770–3.

451   http://www.ncbi.nlm.nih.gov/pubmed/16760982 (Accessed August 20, 2014).

452   Chambeyron S, Bickmore WA. 2004. Chromatin decondensation and nuclear reorganization of the HoxB

453   locus upon induction of transcription. 1119–1130.

454   Chen B, Gilbert L a, Cimini B a, Schnitzbauer J, Zhang W, Li G-W, Park J, Blackburn EH, Weissman JS, Qi LS,

455   et al. 2013. Dynamic imaging of genomic loci in living human cells by an optimized CRISPR/Cas

456   system. *Cell* **155**: 1479–91. http://www.ncbi.nlm.nih.gov/pubmed/24360272 (Accessed July 9,

457   2014).

458   Chuang C-H, Carpenter AE, Fuchsova B, Johnson T, de Lanerolle P, Belmont AS. 2006a. Long-Range

459   Directional Movement of an Interphase Chromosome Site. *Curr Biol* **16**: 825–831.

460   Chuang CH, Carpenter AE, Fuchsova B, Johnson T, de Lanerolle P, Belmont AS. 2006b. Long-Range

461   Directional Movement of an Interphase Chromosome Site. *Curr Biol* **16**: 825–831.

462   Cisse II, Izeddin I, Causse SZ, Boudarene L, Senecal A, Muresan L, Dugast-darzacq C, Hajj B. 2013.

463   Polymerase II Clustering in. *Science (80-)* **245**: 664–667.

464   Dalvai M, Fleury L, Bellucci L, Kocanova S, Bystricky K. 2013. TIP48/Reptin and H2A.Z Requirement for

465   Initiating Chromatin Remodeling in Estrogen-Activated Transcription. *PLoS Genet* **9**.

466   Darzacq X, Shav-Tal Y, de Turris V, Brody Y, Shenoy SM, Phair RD, Singer RH. 2007. In vivo dynamics of

467   RNA polymerase II transcription. *Nat Struct Mol Biol* **14**: 796–806.

468   Darzacq X, Yao J, Larson DR, Causse SZ, Bosanac L, de Turris V, Ruda VM, Lionnet T, Zenklusen D,

469   Guglielmi B, et al. 2009. Imaging transcription in living cells. *Annu Rev Biophys* **38**: 173–196.

470   Feuerborn A, Cook PR. 2015. Why the activity of a gene depends on its neighbors. *Trends Genet* **31**: 483–

471   490. http://dx.doi.org/10.1016/j.tig.2015.07.001.

472   Fullwood MJ, Liu MH, Pan YF, Liu J, Xu H, Mohamed Y Bin, Orlov YL, Velkov S, Ho A, Mei PH, et al. 2009.

473   An oestrogen-receptor-α-bound human chromatin interactome. *Nature* **462**: 58–64.

474   http://www.nature.com/doifinder/10.1038/nature08497.

475   Ghamari A, Tte M, Van De Corput PC, Thongjuea S, Van Cappellen WA, Van Ijcken W, Van Haren J, Soler

476   E, Eick D, Lenhard B, et al. 2013. In vivo live imaging of RNA polymerase II transcription factories in

477   primary cells. 767–777.

478   Giorgetti L, Galupa R, Nora EP, Piolot T, Lam F, Dekker J, Tiana G, Heard E. 2014. Predictive polymer

479   modeling reveals coupled fluctuations in chromosome conformation and transcription. *Cell* **157**:

480   950–963.

481   Graham TGW, Wang X, Song D, Etson CM, van Oijen AM, Rudner DZ, Loparo JJ. 2014. ParB spreading

482   requires DNA bridging. *Genes Dev* **28**: 1228–1238.

483   Gribnau J, de Boer E, Trimborn T, Wijgerde M, Milot E, Grosveld F, Fraser P. 1998. Chromatin interaction

484   mechanism of transcriptional control in vivo. *EMBO J* **17**: 6020–7.

485   http://www.pubmedcentral.nih.gov/articlerender.fcgi?artid=1170928&tool=pmcentrez&rendertyp

486   e=abstract.

487   Haddad N, Jost D, Vaillant C. 2017. Perspectives: using polymer modeling to understand the formation

488   and function of nuclear compartments. *Chromosom Res*. http://link.springer.com/10.1007/s10577-

489   016-9548-2.

490   Hah N, Danko CG, Core L, Waterfall JJ, Siepel A, Lis JT, Kraus WL. 2011. A rapid, extensive, and transient

491   transcriptional response to estrogen signaling in breast cancer cells. *Cell* **145**: 622–634.

492   http://dx.doi.org/10.1016/j.cell.2011.03.042.

493 Hajjoul H, Mathon J, Ranchon H, Goiffon I, Alber B, Gadal O, Bystricky K, Bancaud A. 2013. High

494 throughput chromatin motion tracking in living yeast reveals the flexibility of the fiber throughout

495 the genome. *Genome Res* **23**: 1829–1838.

496 Hancock R. 2004. Internal organisation of the nucleus: assembly of compartments by macromolecular

497 crowding and the nuclear matrix model. *Biol Cell* **96**: 595–601.

498 Hsieh T-HS, Weiner A, Lajoie B, Dekker J, Friedman N, Rando OJ. 2015. Mapping Nucleosome Resolution

499 Chromosome Folding in Yeast by Micro-C. *Cell* **162**: 108–119.

500 http://linkinghub.elsevier.com/retrieve/pii/S0092867415006388.

501 Huet S, Lavelle C, Ranchon H, Carrivain P, Victor JM, Bancaud A. 2014. *Relevance and limitations of*

502 *crowding, fractal, and polymer models to describe nuclear architecture*. 1st ed. Elsevier Inc.

503 http://dx.doi.org/10.1016/B978-0-12-800046-5.00013-8.

504 Jonkers I, Kwak H, Lis JT. 2014. Genome-wide dynamics of Pol II elongation and its interplay with

505 promoter proximal pausing, chromatin, and exons. *Elife* **2014**: 1–25.

506 Kepten E, Weron A, Sikora G, Burnecki K, Garini Y. 2015. Guidelines for the fitting of anomalous diffusion

507 mean square displacement graphs from single particle tracking experiments. *PLoS One* **10**: 1–10.

508 http://dx.doi.org/10.1371/journal.pone.0117722.

509 Kimura H, Sugaya K, Cook PR. 2002. The transcription cycle of RNA polymerase II in living cells. *J Cell Biol*

510 **159**: 777–782.

511 Kocanova S, Kerr EA, Rafique S, Boyle S, Katz E, Caze-Subra S, Bickmore WA, Bystricky K. 2010. Activation

512 of estrogen-responsive genes does not require their nuclear co-localization. *PLoS Genet* **6**.

513 Le Dily FL, Ba?? D, Pohl A, Vicent GP, Serra F, Soronellas D, Castellano G, Wright RHG, Ballare C, Filion G,

514 et al. 2014. Distinct structural transitions of chromatin topological domains correlate with

515 coordinated hormone-induced gene regulation. *Genes Dev* **28**: 2151–2162.

516 Liu X-F, Bagchi MK. 2004. Recruitment of distinct chromatin-modifying complexes by tamoxifen-

517   complexed estrogen receptor at natural target gene promoters in vivo. *J Biol Chem* **279**: 15050–8.

518   http://www.ncbi.nlm.nih.gov/pubmed/14722073 (Accessed October 18, 2014).

519   Ma H, Naseri A, Reyes-Gutierrez P, Wolfe S a., Zhang S, Pederson T. 2015. Multicolor CRISPR labeling of

520   chromosomal loci in human cells. *Proc Natl Acad Sci* 201420024.

521   http://www.pnas.org/lookup/doi/10.1073/pnas.1420024112.

522   Manzo C, Garcia-Parajo MF. 2015. A review of progress in single particle tracking: from methods to

523   biophysical insights. *Reports Prog Phys* **78**: 124601.

524   Métivier R, Penot G, Hübner MR, Reid G, Brand H, Koš M, Gannon F. 2003. Estrogen receptor-α directs

525   ordered, cyclical, and combinatorial recruitment of cofactors on a natural target promoter. *Cell* **115**:

526   751–763.

527   Mitchell JA, Fraser P. 2008. Transcription factories are nuclear subcompartments that remain in the

528   absence of transcription. *Genes Dev* **22**: 20–25.

529   Mourad R, Hsu P-Y, Juan L, Shen C, Koneru P, Lin H, Liu Y, Nephew K, Huang TH, Li L. 2014. Estrogen

530   induces global reorganization of chromatin structure in human breast cancer cells. *PLoS One* **9**:

531   e113354. http://www.ncbi.nlm.nih.gov/pubmed/25470140 (Accessed December 5, 2014).

532   N. Chenouard, I. Bloch JO-M. 2013. Multiple Hypothesis Tracking for Cluttered Biological Image

533   Sequences. *IEEE Trans Pattern Anal Mach Intell* **35**: 2736–3750.

534   Neumann FR, Dion V, Gehlen LR, Tsai-Pflugfelder M, Schmid R, Taddei A, Gasser SM. 2012. Targeted

535   INO80 enhances subnuclear chromatin movement and ectopic homologous recombination. *Genes*

536   *Dev* **26**: 369–383.

537   Ochiai H, Sugawara T, Yamamoto T. 2015. Simultaneous live imaging of the transcription and nuclear

538   position of specific genes. *Nucleic Acids Res* 1–12.

539   http://nar.oxfordjournals.org/lookup/doi/10.1093/nar/gkv624.

540   Osborne CS, Chakalova L, Brown KE, Carter D, Horton A, Debrand E, Goyenechea B, Mitchell J a, Lopes S,

541   Reik W, et al. 2004. Active genes dynamically colocalize to shared sites of ongoing transcription. *Nat*

542   *Genet* **36**: 1065–1071.

543   P. Thévenaz, U.E. Ruttimann MU. 1998. A Pyramid Approach to Subpixel Registration Based on Intensity.

544   *IEEE Trans Image Process* **7**: 27–41.

545   Passot FM, Calderon V, Fichant G, Lane D, Pasta F. 2012. Centromere Binding and Evolution of

546   Chromosomal Partition Systems in the Burkholderiales. **194**: 3426–3436.

547   Robinett CC, Straight A, Li G, Willhelm C, Sudlow G, Murray A, Belmont AS. 1996. In vivo localization of

548   DNA sequences and visualization of large-scale chromatin organization using lac operator/repressor

549   recognition. *J Cell Biol* **135**: 1685.

550   Sanchez A, Cattoni DI, Walter J-C, Rech J, Parmeggiani A, Nollmann M, Bouet J-Y. 2015. Stochastic Self-

551   Assembly of ParB Proteins Builds the Bacterial DNA Segregation Apparatus. *Cell Syst* **1**: 163–173.

552   http://linkinghub.elsevier.com/retrieve/pii/S2405471215000575.

553   Saxton MJ. 2009. Single Particle Tracking. *Fundam Concepts Biophys* 1–33.

554   Sbalzarini IF, Koumoutsakos P. 2005. Feature point tracking and trajectory analysis for video imaging in

555   cell biology. *J Struct Biol* **151**: 182–195.

556   Schuettengruber B, Cavalli G. 2009. Recruitment of Polycomb group complexes and their role in the

557   dynamic regulation of cell fate choice. *Development* **136**: 3531–3542.

558   Shang Y, Hu X, Direnzo J, Lazar MA, Brown M, Endocrinology D. 2000. Cofactor Dynamics and Sufficiency

559   in Estrogen Receptor – Regulated Transcription. **103**: 843–852.

560   Stasevich TJ, Hayashi-Takanaka Y, Sato Y, Maehara K, Ohkawa Y, Sakata-Sogawa K, Tokunaga M, Nagase

561   T, Nozaki N, McNally JG, et al. 2014. Regulation of RNA polymerase II activation by histone

562   acetylation   in   single   living   cells.   *Nature*   **516**:   272–275.

563   http://www.nature.com/doifinder/10.1038/nature13714 (Accessed September 21, 2014).

564   Stavreva D a, Coulon A, Baek S, Sung M, John S, Stixova L, Tesikova M, Hakim O, Miranda T, Hawkins M,

565   et al. 2015. Dynamics of chromatin accessibility and long-range interactions in response to

566   glucocorticoid pulsing. 1–13.

567 Straight AF, Belmont AS, Robinett CC, Murray AW. 1996. GFP tagging of budding yeast chromosomes

568   reveals that protein–protein interactions can mediate sister chromatid cohesion. *Curr Biol* **6**: 1599–

569   1608. http://linkinghub.elsevier.com/retrieve/pii/S0960982202707835.

570 Taddei A, Gasser SM. 2012. Structure and function in the budding yeast nucleus. *Genetics* **192**: 107–129.

571 Taddei A, Van Houwe G, Hediger F, Kalck V, Cubizolles F, Schober H, Gasser SM. 2006. Nuclear pore

572   association confers optimal expression levels for an inducible yeast gene. *Nature* **441**: 774–8.

573   http://www.ncbi.nlm.nih.gov/pubmed/16760983 (Accessed October 9, 2014).

574 Therizols P, Illingworth RS, Courilleau C, Boyle S, Wood AJ, Bickmore WA. 2014. Chromatin

575   decondensation is sufficient to alter nuclear organization in embryonic stem cells. 2–7.

576 Ulianov S V., Khrameeva EE, Gavrilov AA, Flyamer IM, Kos P, Mikhaleva EA, Penin AA, Logacheva MD,

577   Imakaev M V., Chertovich A, et al. 2016. Active chromatin and transcription play a key role in

578   chromosome partitioning into topologically associating domains. *Genome Res* **26**: 70–84.

579 Vispé S, DeVries L, Créancier L, Besse J, Bréand S, Hobson DJ, Svejstrup JQ, Annereau J-P, Cussac D,

580   Dumontet C, et al. 2009. Triptolide is an inhibitor of RNA polymerase I and II-dependent

581   transcription leading predominantly to down-regulation of short-lived mRNA. *Mol Cancer Ther* **8**:

582   2780–2790.

583 Wachsmuth M, Conrad C, Bulkescher J, Koch B, Mahen R, Isokane M, Pepperkok R, Ellenberg J. 2015.

584   High-throughput fluorescence correlation spectroscopy enables analysis of proteome dynamics in

585   living cells. *Nat Biotechnol* **33**: 384–9.

586 Wang R, Mozziconacci J, Bancaud A, Gadal O. 2015. Principles of chromatin organization in yeast:

587   relevance of polymer models to describe nuclear organization and dynamics. *Curr Opin Cell Biol* **34**:

588   54–60. http://linkinghub.elsevier.com/retrieve/pii/S0955067415000447.

589   Yunger S, Rosenfeld L, Garini Y, Shav-Tal Y. 2010. Single-allele analysis of transcription kinetics in living

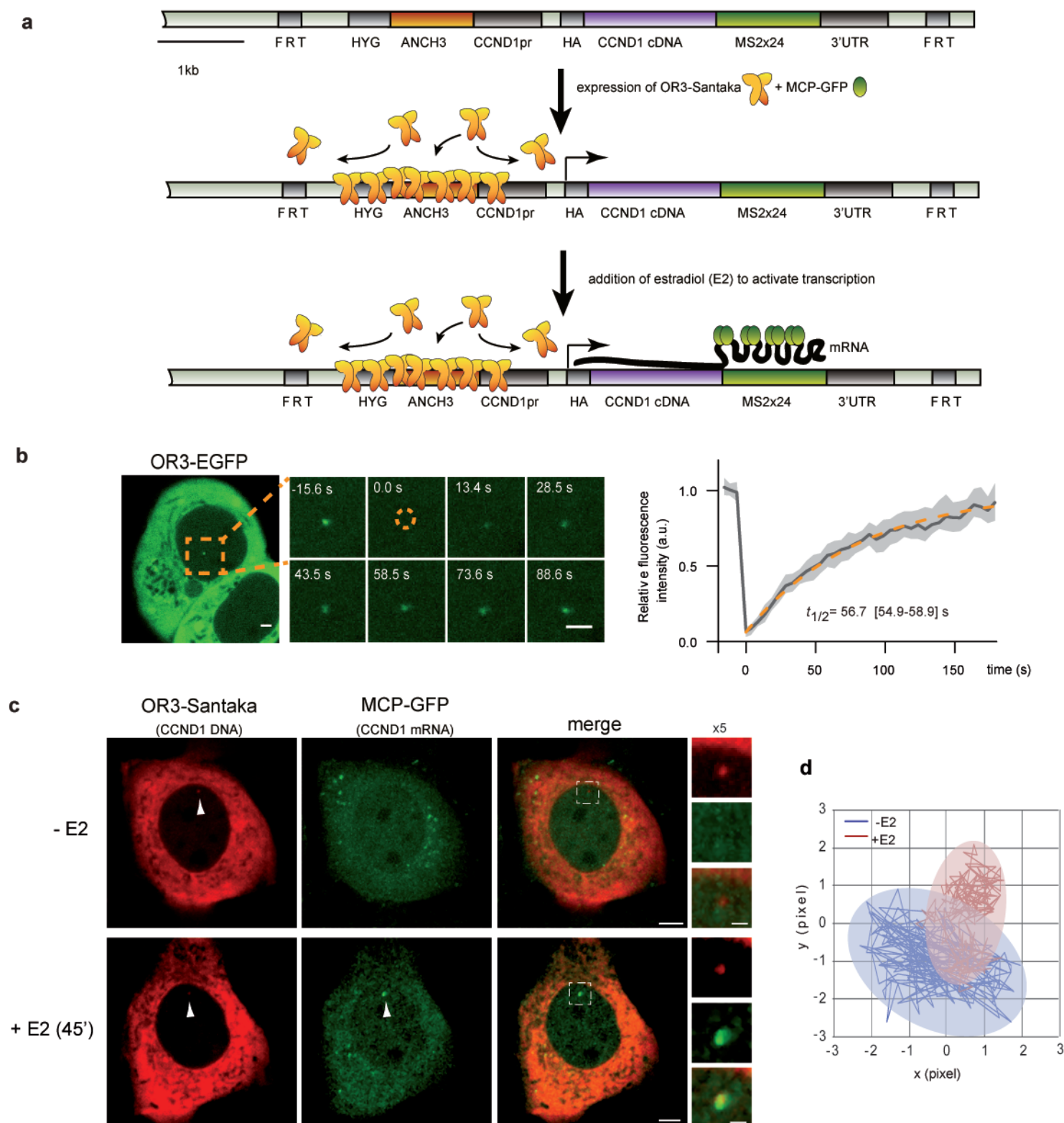590   mammalian cells. *Nat Methods* **7**: 631–633. http://dx.doi.org/10.1038/nmeth.1482.

591

Fig. 1: Real-time visualization of a single Cyclin D1 (CCND1) gene locus in human cells
(a) Schematic representation of a stably inserted construct (ANCH3-CCND1-MS2) comprising the CCND1 gene under its endogenous promoter, adjacent to a unique ANCH3 sequence, 24x MS2 repeats within the 3'UTR and a hygromycin selection gene (HYG). The construct is flanked by FRT sites for integration into MCF-7 FRT cells. Transient transfection with OR3 and MCP-tagged fluorescent proteins results in their accumulation at the ANCH3 and MS2 sequences (after estradiol (E2) stimulation), respectively (raw 3D images in supplemental video 1). (b) Fluorescent spots are easily detectable in transfected cells. A representative cell with an OR3-EGFP spot is shown. Region imaged during fluorescence recovery after photobleaching (FRAP) is indicated in orange. At time t=0s a circular region enclosing the ANCHOR spot was bleached and fluorescence recovery of the spot was followed over time. Relative fluorescence intensity (RFI) was calculated according to (see Materials and methods online and Fig. S1; right panel; solid line: mean, shadowed region: lower and upper quartile; n = 44 cells, 4 experiments with n ≥ 6 cells per experiment). Data were fitted to a single exponential. The 95% confidence interval is indicated in brackets. Scale bar: 2 µm. (c) Representative images of transiently transfected ANCH3-CCND1-MS2 cells expressing OR3-Santaka and MCP-EGFP (raw images in videos S1, S2). CCND1 DNA (red spot) colocalizes with transcribed mRNA (green spot) as MCP-EGFP associates with MS2 stem loops 45min after adding 100nM estradiol (E2). The same cell is shown before and after addition of E2. Scale bar = 5µm and 2µm (for cropped images). (d) Example of 2D trajectories and area explored over 50s (250ms acquisition, 200 steps) of the OR3-Santaka labeled CCND1 locus recorded before (-E2) and after (+E2) transcription activation.
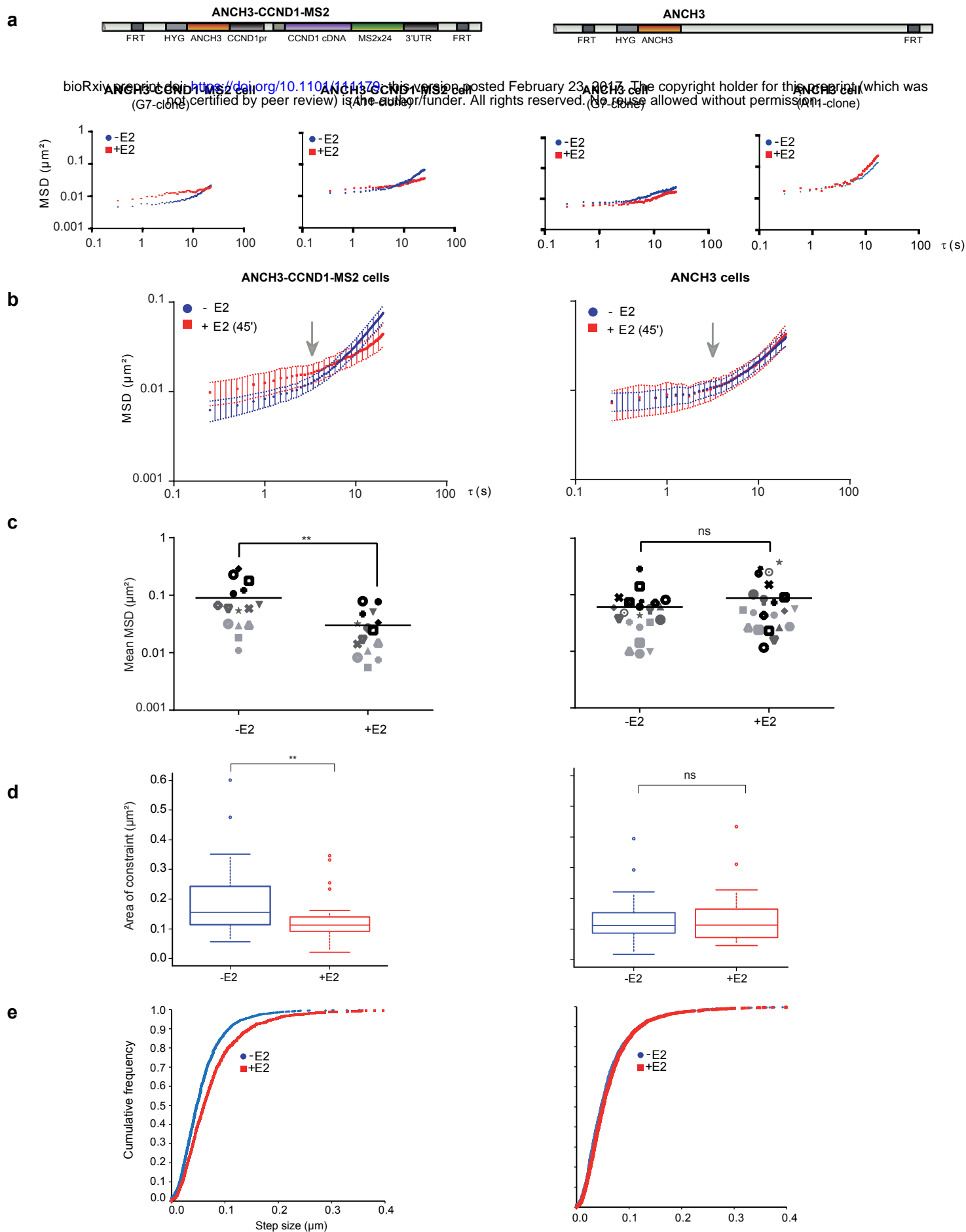
Fig. 2: Cyclin D1 motion is confined during estradiol induced transcription activation.
(a) Representative single cell MSD curves of OR3-Santaka loci in ANCH3-CCND1-MS2 and ANCH3 cells at two different chromosomal insertion sites (clones G7 and A11; distinct stable FRT insertions in MCF-7 cells) before and 45 minutes after E2 addition. (b) Averaged MSD curves of OR3-Santaka loci tracking in ANCH3-CCND1-MS2 (n=14) and ANCH3 (n=14) cells before and after E2 addition. The arrow indicates the 5 s time point separating two diffusive regimes (Fig. S4 b). (c) Average squared displacement between 2 s and 40 s (mean MSD) of tracking of the OR3-Santaka spot in ANCH3-CCND1-MS2 cells (left panel, n=15, p-value=0.006) and ANCH3 cells (right panel, n=21, p-value=0.3) before and 45 min after E2 addition. (d) Area of constraint of the OR3-Santaka locus in ANCH3-CCND1-MS2 cells (left panel, n=24, p-value=0.006) and ANCH3 cells (right panel, n=20, p-value=0.860) before and after E2 addition. The boxes show the median and 25–75 percentiles of the data. Asterisks indicate data points beyond the 95th percentile. Student's t-test: *P-values: >0.05 (ns), <0.05 (*), <0.01 (**), <0.001 (***), <0.0001 (****). (e) Cumulative distribution function of CCND1 loci step size in ANCH3-CCND1-MS2 cells (left panel, n=14, p-value<0.001) and ANCH3 cells (right panel, n=14, p-value=0.03) before and after E2 addition.
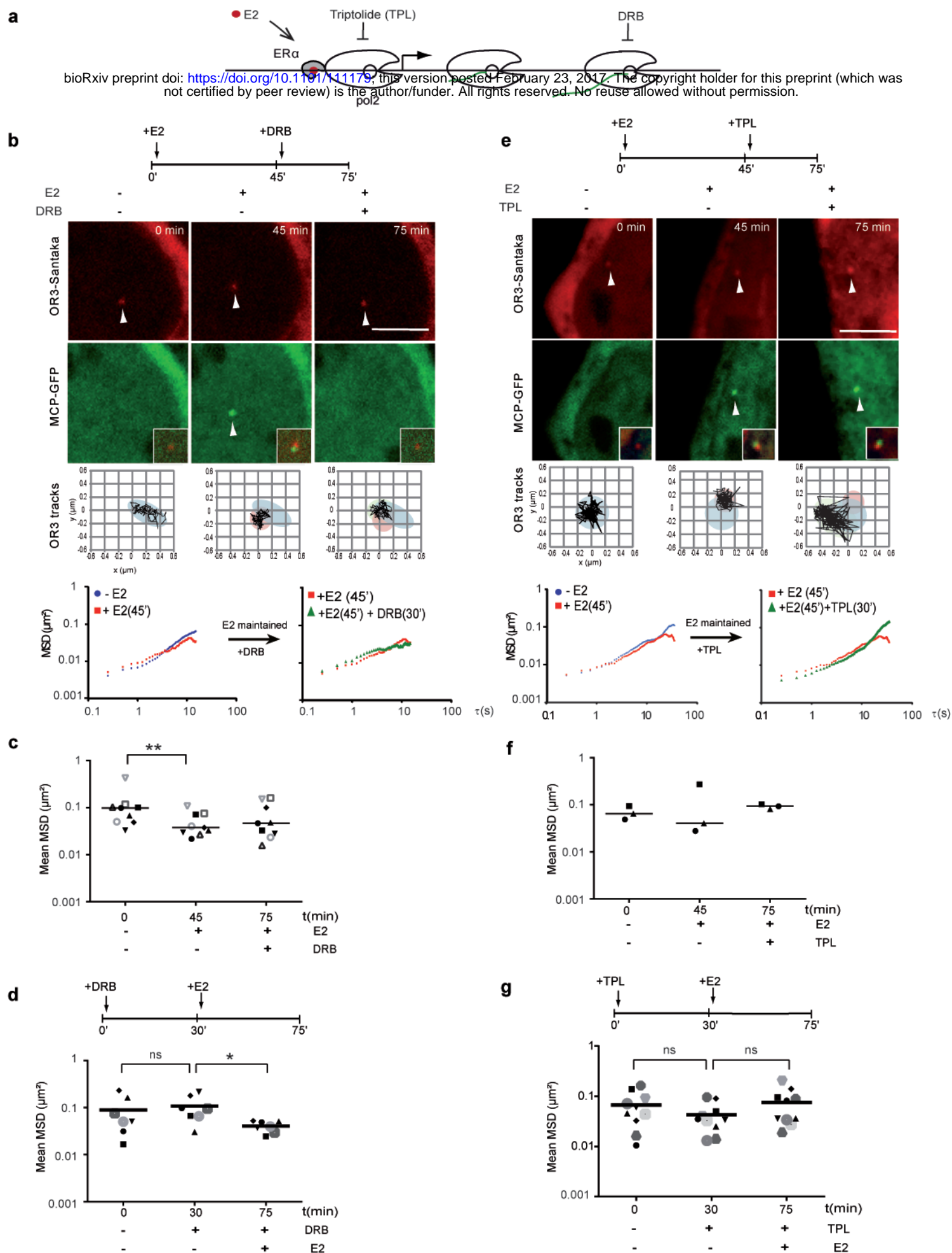
Fig.3: Transcription initiation but not elongation confines chromatin motion.
(a) Schematic representation of the steps of the E2-induced ERα-bound CCND1 the inhibited by Triptolide and DRB during transcription initiation or elongation, respectively. (b, e) Experimental set-up, 100 nM of E2 was used to activate transcription and 50 μM DRB to block elongation (b) or 500 nM of Triptolide (TPL) to block initiation of transcription (e). The CCND1 locus was tracked at time points before and after treatment as specified. Representative images from live cell imaging of ANCH3-CCND1-MS2 cells (clone G7) treated first with E2 for 45 min and then with DRB or TPL for 30 min, respectively (b, e). mRNA production is activated by E2 and then blocked by inhibiting transcription elongation as evidenced by the appearance and disappearance of the MCP-EGFP signal. Scale bar = 5 μm. Successive positions of the OR3-Santaka spot are displayed in the bottom squares (122 steps, 250 ms interval). Representative single cell MSD curves of OR3 loci detected in a cell treated with E2 and then DRB. (c) Average squared displacement between 2 s and 40 s (mean MSD) of single cells (n=9) treated successively with E2 and then DRB. (d) Mean MSD (250 ms interval, 200 steps, n=7) of single cells pre-treated with 50 μM DRB for 30 min (p-value=0.578) and then treated with 100 nM E2 for 45 min (p-value=0.031). (e, f) as (b, c), but after timed treatment with TPL. (g) Mean MSD (250 ms interval, 200 steps, n=10) of single cells pre-treated with 500 nM TPL for 30 min (p-value=0.117) and then treated with 100 nM E2 for 45min (p-value=0.065).

	Treatment	Area of confinement (µm²)					Speed (µm/s)				
		0 min	30 min	45 min	75 min	105 min	0 min	30 min	45 min	75 min	105 min
ANCH3-CCND1-MS2 cells	all E2	0.175 ±0.119 N=63		0.117 ±0.06 N=34 (E2)			0.255 ±0.085 N=63		0.293 ±0.131 N=34 (E2)		
	E2 (45')	0.195±0.134 N=24		0.133±0.082 (E2)			0.231 N=14		0.304 (E2)		
	E2 (105')	0.106 ±0.05 N=4		0.106 ±0.06 (E2)	0.129 ±0.06 (E2)	0.101 ±0.05 (E2)	0.260		0.263 (E2)	0.261 (E2)	0.323 (E2)
	(E2+DRB)	0.143 ±0.054 N=8		0.121±0.041 (E2)	0.172±0.150 (E2+DRB)	0.173±0.106 (E2+DRB)	0.215		0.246 (E2)	0.259 (E2+DRB)	0.318 (E2+DRB)
	(DRB+E2)	0.163±0.075 N=7	0.254±0.114 (DRB)		0.205±0.24 (DRB+E2)		0.276	0.270 (DRB)		0.305 (DRB+E2)	
	E2 then DRB	0.155 ±0.033 N=3		0.123 ±0.039 (E2)	0.124 ±0.036 (DRB)	0.163 ±0.040 (DRB)	0.227		0.269 (E2)	0.251 (DRB)	0.308 (DRB)
	DRB (105')	0.148 ±0.040 N=5		0.190 ±0.064 (DRB)	0.160 ±0.058 (DRB)	0.109 ±0.061 (DRB)	0.262		0.273 (DRB)	0.341 (DRB)	0.306 (DRB)
	(E2+TPL)	0.154±0.057 N=3		0.099±0.045 (E2)	0.213±0.055 (E2+TPL)	0.168±0.016 (E2+TPL)	0.321		0.417 (E2)	0.330 (E2+TPL)	0.333 (E2+TPL)
	(TPL+E2)	0.219±0.189 N=10	0.143±0.083 (TPL)		0.253±0.179 (TPL+E2)		0.296	0.288 (TPL)		0.321 (TPL+E2)	
	no treatment	0.118 ±0.035 N=6		0.112±0.066	0.126±0.068	0.085±0.053	0.253		0.251	0.271	0.236
ANCH3 cells	E2 (45')	0.132±0.090 N=20		0.137±0.096 (E2)			0.242 N=14		0.256 (E2)		

Table 1:

Summary of confined areas and speeds calculated for different treatments. Data are shown as average +/- standard deviation. The first line contains all cells that were not treated (0min, n=63) or treated 45 min with E2 (45min, n=34), independently of the rest of experiment.